Catalysis Science & Technology

Accepted Manuscript

ROYAL SOCIETY OF CHEMISTRY

www.rsc.org/catalysis

Single molecule study of samarium oxide nanoparticles as a purely heterogeneous catalyst for one-pot aldehyde chemistry

Gregory K. Hodgson, Stefania Impellizzeri*, and Juan C. Scaiano*

Department of Chemistry and Biomolecular Sciences and Centre for Catalysis Research and Innovation, University of Ottawa, 10 Marie Curie, Ottawa, Ontario, Canada K1N 6N5.

Correspondence and requests for materials should be addressed to J.C.S. (email: scaiano@photo.chem.uottawa.ca)

Abstract

Heterogeneous catalysis holds distinct advantages over homogeneous catalysis; however, it is only truly advantageous if unaffected by metal ion leaching or *in situ* formation of a soluble catalytically active species. Herein, samarium oxide nanoparticles (Sm_2O_3NP) were employed as a redox catalyst for the first time, providing a generally applicable route to performing one-pot aldehyde chemistry beginning with an inexpensive and more readily-prepared starting material – an alcohol. The reaction is efficient under mild conditions and does not suffer from over-oxidation of the starting material to its corresponding carboxylic acid. This key asset of the Sm_2O_3NP catalyst hinges upon a lack of release of free aldehyde into the system. Single molecule fluorescence microscopy revealed that catalysis is restricted to the surfaces of small nanoparticles in a polydisperse nanomaterial, where the product of the oxidative process can be selectively revealed via a subsequent coupling reaction, which occurs without the intermediacy of a free aldehyde. Instead the catalytically active particles act as docking stations, holding the

pre-aldehyde until intercepted by a second reagent to complete the oxidation and subsequent reaction in a single step. Coupling this supramolecular strategy to our single molecule approach revealed the interesting nature of the catalytic mechanism and demonstrated that the catalysis is a purely heterogeneous process. Samarium is quite abundant relative to many transition metals (e.g. Ru, Ir, Pt) and thus Sm_2O_3NP-based nanomaterials may present an opportunity to develop more sustainable catalysts for common organic transformations.

Introduction

In recent years, single molecule fluorescence microscopy has become a valuable tool in the study of chemical reactions, providing fundamental mechanistic insights for their development and improvement.[1-19] In the context of transition metal and metal nanoparticle (NP) catalysis, single molecule techniques offer a means to determine the true nature of the catalysis, whether it be homogeneous, heterogeneous or some combination that defies traditional classification.[20-24] For example, Blum and co-workers used single molecule fluorescence microscopy to demonstrate the homogeneous nature of a ruthenium catalyst by imaging a ring-opening metathesis polymerization (ROMP).[25, 26] In a recent report, we employed Total Internal Reflection Fluorescence Microscopy (TIRFM) to establish that copper nanoparticles (CuNP) can effectively promote the 1,3-dipolar cycloaddition between an azide and a terminal alkyne (click chemistry) through a purely heterogeneous pathway.[27] Discerning the active regions of catalysts is also of great interest, and has been the focus of a number of recent single molecule catalysis reports.[1, 2, 18] Hofkens and co-workers successfully used single molecule techniques to map the catalytic activity of zeolites and mesoporous materials.[10, 13-15] The field has progressed to a stage in which single molecule–single particle studies yield enough information to improve the performance of a catalytic system at the bench scale, through heterogenization of the catalytic process or by

describing how key aspects of catalyst preparation or modification impact its activity, or the mode by which the catalysis proceeds.[2-4, 10, 13, 14, 25, 26]

Single molecule techniques also offer the opportunity to evaluate the performance and the behavior of a catalyst when conventional bench scale techniques are inadequate or not applicable. For instance, they can provide a useful alternative to large scale catalyst production in situations where catalyst preparation requires lengthy procedures, harsh experimental conditions or gives low yields. Providing that the synthesis of the material does not present safety concerns or other drawbacks, catalysts are routinely synthesized in relatively large quantities and catalytic activity is assessed at the bench scale through screening of multiple reagents and reaction conditions, often accompanied by high throughput combinatorial analysis. However, this trial and error approach becomes vastly inefficient when catalyst or reagent preparation is particularly challenging, costly or scarcely efficient. Single molecule fluorescence microscopy circumvents these obstacles by providing a viable alternative; it is a bottom-up approach permitting the examination of catalytic activity when traditional approaches are limited, and thereby extends the realm of possibilities in catalysis research.

We recently developed a simple and safe synthetic strategy for the photochemical preparation of samarium oxide nanoparticles (Sm_2O_3NP) under mild conditions.[28] Within this contribution, we reported for the first time that Sm_2O_3NP possess Brønsted-type acidity. Although our synthetic protocol offers several advantages with respect to previously reported methods, the low percent yield obtained did not allow for a systematic screening of substrates to investigate the catalytic performance of Sm_2O_3NP. Nevertheless, using single molecule microscopy, we were able to investigate the activity of these Sm_2O_3NP utilizing very low quantities of catalyst. We have already examined one potential application of this new material

in the Brønsted acid catalyzed synthesis of coumarin dyes via the Pechmann *trans*-esterification and condensation pathway.[22] Although the process produced high yields for several catalytic cycles under mild conditions, monitoring the catalysis at the single molecule level revealed startling information on the catalyst performance and potential for scaled up synthesis. TIRFM demonstrated that the active species is in fact comprised of smaller NP present in the polydisperse solid nanomaterial, and that the reaction occurs heterogeneously on the surfaces of these colloidal NP. Despite the ability to separate the catalyst by increasing the ionic strength of the solution after the reaction, we elected to act on the insight provided by single molecule fluorescence microscopy, and investigate other catalytic systems where the behaviour of the Sm_2O_3NP might be improved upon in order to take full advantage of pure heterogeneous catalysis. The supramolecular system described here achieved this objective by increasing the ionic strength of the reaction mixture enough to maintain phase-separation between the product and the catalytically active nanoparticles. We refer to this strategy of building upon information gained at the single molecule level to improve bench scale catalytic performance as *'from the molecule to the mole'*.

Herein, we sought to determine whether Sm_2O_3NP can be employed as a redox catalyst for the purpose of conducting one-pot aldehyde chemistry beginning with a more readily prepared and inexpensive starting material – the corresponding alcohol. The electronic configuration of samarium is highly responsive to small changes in the local chemical environment, and this sensitivity may be responsible for the interesting diversity of surface and subsurface oxidation states observed in different samarium-based nanomaterials.[29] Efforts to understand the nature of these valence changes as they relate to temperature, particle size, morphology and composition have suggested that while in most cases the Sm^{3+} oxidation state

dominates over Sm^{2+}, mixed valences are likely to exist on the surfaces of samarium-based nanomaterials.[30-35] Whether these mixed valences are of a homogeneous (Sm_2O_{3-x}) or heterogeneous (site specific integer valence) nature is still unknown for the general case, and may well be a material-specific property.[30] Regardless of their source, such oxygen deficiencies can allow for the capture and release of oxygen under redox conditions, a quality that has garnered some interest for the development and characterization of samarium-based redox catalysts.[32-34, 36] To the best of our knowledge, this report is the first example in which Sm_2O_3NP have been investigated for redox-type catalysis. Partial oxidation of the starting alcohol occurs on the surfaces of Sm_2O_3NP, and thus the catalytic nanoparticles also act as protective docking stations for the activated alcohol until it can be intercepted by another reagent to complete the oxidation and subsequent reaction in one-pot. This strategy allows the synthesis of aldehyde-derived compounds to proceed without the intermediacy of a free aldehyde and prevents over-oxidation to the carboxylic acid, a common problem in aldehyde oxidation chemistry. The supramolecular strategy employed herein not only improved upon our previous work by ensuring that the catalytic process is fully heterogeneous, it also offered a facile means to monitor yields at the bench scale and at the single molecule level (*vide infra*).

Results

Benchtop Experimentation. In order to investigate the Sm_2O_3NP-catalyzed oxidation of alcohols both at the bench scale and at the single molecule level, we synthesized the –OH functionalized fluorescent compound **1** (Figure 1). Compound **1** absorbs at 380 nm and is strongly emissive at 450 nm; by replacing the hydroxyl functionality with an aldehyde as in compound **2**, both the absorption and emission wavelengths shift to 450 and 490 nm, respectively (Figure S1-S2, Supporting Information). Interestingly, the emission spectrum of the

supernatant obtained by centrifuging (3000 rpm, 30 min) a solution of Sm_2O_3NP and **1** previously stirred for 24 h at 65°C contains an emission band centered at 465 nm (Figure S3, Supporting Information). This band is slightly red-shifted with respect to **1** (at 450 nm) and blue-shifted with respect to **2** (at 490 nm) but is still consistent with a coumarin-type structure, which we refer to as the partially oxidized activated alcohol compound on the Sm_2O_3NP surface (abbreviated "$\mathbf{[2]_s}$"). However, this red shift is insufficient to permit estimation of the yield of $\mathbf{[2]_s}$ obtained in the reaction by spectroscopic methods. Only upon addition of an equimolar amount of **3** (relative to **1**) were we able to estimate the yield of both $\mathbf{[2]_s}$ and **4**, using absorbance spectroscopy. Compound **3** is unreactive toward the –OH functional group but reacts with aldehydes in EtOH to generate the supramolecular assembly **4** (Figure 1) in a single step, with quantitative yields and without the addition of a catalyst.[37] In a previous report, we elucidated the mechanism for this condensation.[38]

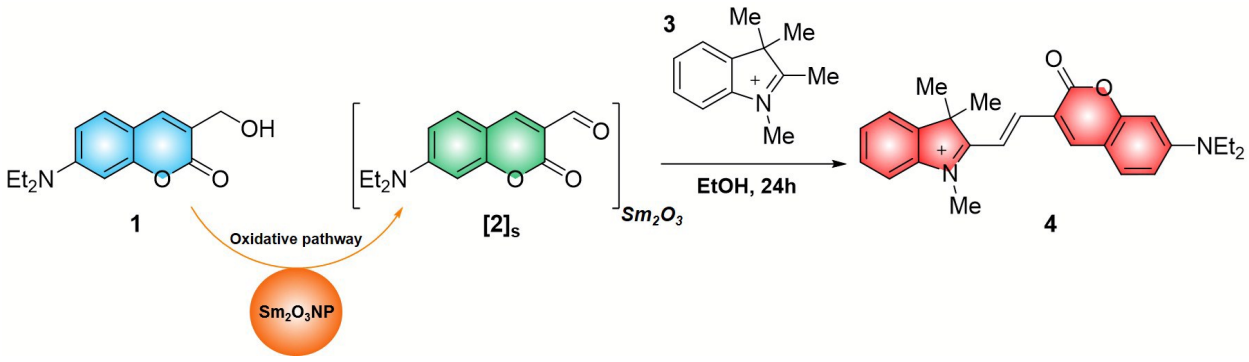

Figure 1 Proposed scheme for the Sm_2O_3NP-catalyzed oxidation of **1** to the activated alcohol compound $\mathbf{[2]_s}$ and its subsequent reaction with the indolium cation **3** to yield the supramolecular assembly **4**.

The extended conjugation within **4** causes a substantial red-shift to the absorption and emission bands of this compound, with the absorption band centered at 575 nm and the emission band at 635 nm. The full spectroscopic characterization of compounds **1**, **2** and **4** is illustrated in Figure S1 and Figure S2 of the Supporting Information. Since the condensation between $\mathbf{[2]_s}$ and **3**

occurs quantitatively, the percent yield of **4** indirectly corresponds to the oxidation of **1** and yield of $\mathbf{[2]_s}$ obtained during the Sm_2O_3NP-catalyzed oxidation of **1**. Knowing that the molar extinction coefficient of **4** is 14218 M^{-1} cm^{-1} at 575 nm, the yield of $\mathbf{[2]_s}$ can easily be estimated by monitoring the appearance of the absorption band of **4**, as illustrated in Figure S1.

For a typical reaction, 12 mg of **1**, 9 mg of **3** and variable amounts of Sm_2O_3NP were dissolved in 2 mL of EtOH and stirred for 24 h at 65 °C. High temperature is not explicitly necessary but encourages the condensation between $\mathbf{[2]_s}$ and **3** (Table 1). The known Brønsted acidity of the Sm_2O_3NP[28] does not affect the reagents' stability nor their activity. In order to maximize the recovery of **4**, the catalyst was centrifuged and washed three times with EtOH and the supernatants combined and dried under reduced pressure. The residue was then dissolved in 2 mL of EtOH, diluted 100 fold and analyzed by UV-Vis spectroscopy. The results are summarized in Table 1.

Table 1 Catalytic performance of Sm_2O_3NP under various reaction conditions. Percent yields of the Sm_2O_3NP-catalyzed oxidation of **1** to $\mathbf{[2]_s}$ were obtained by monitoring the condensation reaction (24 h) between $\mathbf{[2]_s}$ and **3** to generate the supramolecular assembly **4**. For entries **a-h**, mol % reflects the amount of polydisperse Sm_2O_3NP. For entries **i-j**, the amount is given as mol % catalytically active small Sm_2O_3NP isolated from the polydisperse nanomaterial. For entry **g**, the reaction vessel was purged but Ar (g) was not bubbled through the solution and the ethanol solvent was not distilled.

Reaction	Amount of Catalyst	Temperature (°C)	Atmosphere	% yield of **4**
a	1.5 mg (8.9 mol %)	65	air	13
b	1.5 mg (8.9 mol %)	65	O_2	19
c	2 mg (12 mol %)	65	air	27
d	5 mg (30 mol %)	65	air	51
e	No catalyst	65	air	5
f	No catalyst	65	O_2	5
g	5 mg (30 mol %)	65	Ar	48
h	5 mg (30 mol %)	25	air	38
i	2 mL supernatant (3.4 mol %)	25	air	33
j	2 mL supernatant (3.4 mol %)	65	air	51

The results reported in Table 1 indicate that Sm_2O_3NP promote the catalytic oxidation of the hydroxyl-functionalized **1**. Indeed, the generation of **4** should indicate the presence of **[2]$_s$**, because the active methylene in **3** is not reactive toward hydroxyl functionalities. The presence of **4** is thus an indirect confirmation of the successful oxidation of **1**. Oxygen may enhance the performance of the catalyst slightly, as control experiments conducted in the absence of Sm_2O_3NP are not affected by the reaction atmosphere. However, O_2 (g) is not explicitly necessary (compare reactions **d** and **g**, Table 1). An SEM image of Sm_2O_3NP recovered after reaction **d** (Figure S4, Supporting Information) shows that some intact spherical structures are still observable. This observation seems to suggest that the catalyst could potentially be reused but that some degradation occurs, leading to a lesser performance after the first cycle. Recyclability tests for reaction **d** yielded 14.4 % of **4** for a second cycle and 9.8 % for a third cycle. Most likely the low degree of reusability is due to catalyst degradation (as possibly suggested by SEM images) and the loss of the small nanoparticles responsible for most of the catalysis (*vide infra*).

Our results show that Sm_2O_3NP are unable to fully oxidize alcohols and release free aldehyde product. However, Sm_2O_3NP are capable of forming the partially oxidized activated alcohol compound **[2]$_s$**; this in fact may be Sm_2O_3NP' greatest asset, as it effectively prevents over-oxidation to the carboxylic acid, while **[2]$_s$** shows enough aldehyde-like reactivity to be scavenged by **3**. It is intriguing how Sm_2O_3 is capable of oxidizing **1** to **[2]$_s$** in the absence of oxygen (see Table 1). We suggest that in this case Sm_2O_3 acts as a sacrificial oxidant to form **[2]$_s$** followed by its facile recovery (or re-oxidation) by air or oxygen *in situ* or during post-reaction handling. In fact, this is fully consistent with previous reports of samarium oxide materials reversibly alternating between stable Sm_2O_3 and SmO surface states[28-34] and also with our own

observations during the synthesis of Sm_2O_3NP,[28] where ketyl radicals partially reduce Sm^{3+} (most likely never fully reduced to Sm^0), that spontaneously undergoes air oxidation to Sm_2O_3 and over a period of time forms Sm_2O_3NP. Thus, it is not surprising that if the Sm_2O_3 surface undergoes some reduction to SmO through the process shown in Figure 1, it can readily revert to Sm(III) (see also Figure S5 of the Supporting Information).

We have recently reported on another catalytic system, in which the Brønsted acidity of Sm_2O_3NP was exploited in the synthesis of a coumarin dye.[22] Although the catalysis occurred heterogeneously on the surfaces of small Sm_2O_3NP present in the polydisperse nanomaterial, we demonstrated that the catalytically active particles formed a stable colloidal suspension which required the addition of a suitable salt in order to facilitate separation of the catalyst after the reaction. Based on the results of that investigation, and the similar reaction conditions employed here (solvent and temperature) for one-pot aldehyde redox chemistry, we tested for the presence of colloidal Sm_2O_3NP in the reaction mixture to establish the potentially different catalytic roles played by small versus large Sm_2O_3NP. In this case, the previously-reported colloidal stability of Sm_2O_3NP in EtOH did not set any limitation upon the potential to utilize pure heterogeneous catalysis; the supramolecular catalytic system benefitted from the ionic strength provided by cationic compounds **3** and **4**, which kept the zeta potential of the Sm_2O_3NP low enough that they remained in the solid phase during the reaction and did not form a stable colloidal suspension. This was confirmed by the formation of a pellet comprised of Sm_2O_3NP upon centrifugation (30 min at 3000 rpm), after a reaction was performed in which the solid polydisperse nanomaterial and solvent were replaced with supernatant containing only the small Sm_2O_3NP in an initially stable colloidal suspension in EtOH (as in reaction **i**, Table 1). The latter was obtained by stirring

the polydisperse Sm_2O_3NP in EtOH for 24 h at 65°C, centrifuging at 3000 rpm for 30 min, and collecting the supernatant.

Similar to our previous report, a combination of bench scale and single molecule experiments revealed that the small Sm_2O_3NP are the sole catalytically active species. This was initially suggested by the fact that identical yields of **4** (51%) were obtained when the reaction was performed using either the polydisperse solid nanomaterial or the solution of supernatant containing only the sub-population of small Sm_2O_3NP able to form a stable colloidal suspension when an identical mass of polydisperse Sm_2O_3NP powder was pre-exposed to an identical volume of EtOH under reaction conditions (Table 1 reaction **i** vs. **d**). More direct evidence was provided by single molecule experiments carried out using TIRFM (*vide infra*), which conclusively demonstrated that the catalytic oxidation of compound **1** performed by the small (and not the large) Sm_2O_3NP is a heterogeneous process. Poor recovery of this minute fraction of active component could also have contributed to the low degree of catalyst recyclability that was observed. Indeed, a high loading (30 mol %) of the polydisperse nanomaterial was required in order to provide a sufficient number (3.4 mol %) of the catalytically active small nanoparticles required to obtain an acceptable yield.

Distinguishing pure heterogeneous catalysis from homogeneous catalysis, or a mixture of the two processes, is a critical step in the evaluation of new catalytic materials.[11, 17, 20-25, 27, 39] A typical absorption spectrum for a reaction is illustrated in Figure S1 of the Supporting Information. The spectrum shows that both the starting material **1** and the product **4** are present in the reaction mixture, and also suggests traces of the absorption band of $\mathbf{[2]_s}$, consistent with the emission of $\mathbf{[2]_s}$ detected in the supernatant (containing no large inactive Sm_2O_3NP) obtained by centrifugation (3000 rpm, 30 min) of a solution of **1** and Sm_2O_3NP previously stirred for 24 h

at 65°C (Figure S3, Supporting Information). Unfortunately, standard chromatographic techniques did not allow for effective isolation or quantitation of compound **[2]$_s$** from this solution. However, adding compound **3** afterward and stirring the mixture for an additional 24 h at 65°C resulted in the formation of the fully condensed species **4** (14%), indicating that the partially oxidized activated alcohol saturated the surfaces of the small, active Sm_2O_3NP where it was protected from over-oxidation and simply waiting to react with **3**. The lower yield obtained was likely due to a partial loss of unreacted **1** during centrifugation and removal of the large Sm_2O_3NP prior to the addition of **3**.

Although the inability to detect **[2]$_s$** by HPLC suggested that it exists strictly on the surfaces of colloidal Sm_2O_3NP stable in EtOH in the absence of **3**, the details of its role in the overall reaction mechanism remained unclear. While bench scale experimentation did show that only a small sub-population of the polydisperse nanomaterial was catalytically active, it provided no concrete insight into the overall reaction mechanism. We therefore turned to single molecule fluorescence microscopy, which unequivocally demonstrated that the mechanism proceeds via the heterogeneously-catalyzed oxidation of compound **1** to **[2]$_s$** exclusively on the surfaces of small Sm_2O_3NP, where the partially oxidized activated alcohol is then intercepted by compound **3** to generate **4** without the intermediacy of a free aldehyde.

Single Molecule Fluorescence Microscopy. In order to establish the mode of catalysis at work and to elucidate the mechanistic details of the Sm_2O_3NP-catalyzed oxidation of **1**, we investigated the reaction at the single molecule level using TIRFM. The supramolecular strategy employed to monitor the oxidation of **1** at the bench scale provided an additional benefit, by red-shifting the emission band of the product of interest such that it could be selectively excited and

its emission easily distinguished from that of **1** at the single molecule level. The emission band of $\mathbf{[2]_s}$ (at 465 nm, Figure S3, Supporting Information) is too close to that of **1** (Figure S2, Supporting Information) to allow for reliable differentiation via TIRFM and, at the single molecule level, excitation of $\mathbf{[2]_s}$ using a 488 nm light source does not rule out simultaneous excitation of small populations of **1**. However, species **4** possesses strong emission at 635 nm. Selective excitation of **4** at 633 nm allowed its fluorescence to be monitored using a 676/29 nm band pass emission filter, thus providing a reliable and efficient means of obtaining significant insights into the catalyst's behaviour which, although inaccessible using bench scale techniques, could be gained by monitoring the reaction using TIRFM. Experiments were conducted by recording TIRFM image sequences of various lengths while flowing an equimolar mixture (1–5 nM) of **1** and **3** in EtOH atop a glass microscope coverslip spin-coated with Sm_2O_3NP. A representative image sequence is illustrated in Supplementary Video S1.

Analysis of TIRFM image sequences revealed repetitive fluorescence bursting events (sharp jumps in intensity) at discrete locations in the 80×80 μm^2 TIRFM field of view, which can easily be distinguished above a baseline consisting of background scattering and dark counts (Figure 2 and Figure S6, Supporting Information). Individual bursting events are caused by the activation of fluorescence as single molecules of species **4** are formed at specific locations. The recorded intensity spikes when emission from a single molecule is detected in a 3×3 pixel region of interest and subsequently returns to the baseline as the molecule diffuses away, assisted by the continuous flow of reagents and solvent. It follows that the detection of multiple distinct bursts at a given location signifies the precise coordinates of a catalytic site provided by a stationary Sm_2O_3NP, and corresponds to a heterogeneous catalytic process in which no free aldehyde species is released.[18, 22, 27] In contrast, non-catalytic or homogeneously catalyzed formation of

molecules of **4** in solution is manifested as singular bursting events within defined regions of interest, as single molecules diffuse in and out of the focal plane. This is likely to occur more frequently as the concentration of reagents increases, and so when attempting to distinguish between homogeneous and heterogeneous catalysis it is necessary to establish a concentration range in which a satisfactory number of repetitive, co-located bursting events can be observed without causing an overwhelming number of singular bursts to be detected.[13] In this system, many cases of repeated bursting were indeed observed over catalytic Sm_2O_3NP for reagent concentrations ranging from 1 to 5 nM (Figure 2). In order to confirm that the selected bursts belong to the emissive species **4**, we recorded their emission spectrum with an Andor spectrograph coupled to our single molecule microscope system (Figure S7, Supporting Information). The signal was recorded by passing the epifluorescent signal through the spectrograph (λ_{Ex} = 637 nm) and using a 690/70 nm band pass emission filter installed into the Fluorescent Lifetime Imaging (FLIM) system.

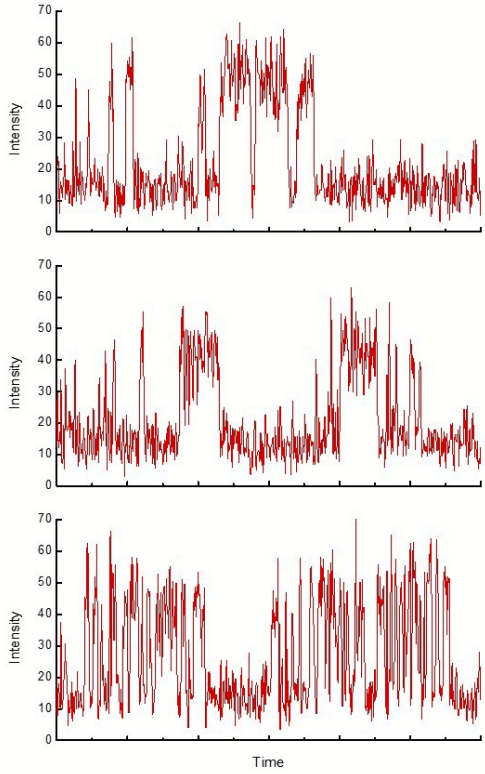

Figure 2 Emission bursting events from single molecules of species **4**. Representative 60 second excerpts from intensity-time trajectories corresponding to 3×3 pixel regions of interest in 100-200 second TIRFM image sequences recorded at room temperature while flowing an equimolar solution of 5 nM **1** and **3** atop a microscope coverslip spin-coated with Sm_2O_3NP. Exposure time was 100 ms per frame. Repetitive bursting at each location is indicative of heterogeneous catalysis. Note the consistent intensity of individual bursts, which each represent fluorescence emission from a single molecule of species **4**.

Using TIRFM, it was also possible to observe and compare the catalytic activity exhibited by small and large Sm_2O_3NP, both known to be present in the polydisperse nanomaterial (Figure S8, Supporting Information).[22] High levels of scattering by large Sm_2O_3NP cause excitation light to impinge upon the emission filter at various angles, rendering such particles visible in TIRFM image sequences. The locations of these large particles can be confirmed via correlation with a widefield transmission image of the same sample area (Figure S9, Supporting Information). Repetitive bursting was observed in various locations in the

TIRFM field of view but importantly, it was never observed atop nor in the immediate vicinity of visually identifiable larger Sm_2O_3NP. This remained the case even when burst localization was preceded by further reduction of scattering through frame by frame subtraction of a background image sequence recorded while flowing only solvent atop the same sample of catalyst before seamlessly switching to an equimolar flow of reagents. This procedure was facilitated by the fact that the degree of scattering due to large Sm_2O_3NP remains relatively constant over the time scale of TIRFM experiments (Figure S10, Supporting Information). Even if catalytic bursting atop the large Sm_2O_3NP were still completely masked by scattering, one would expect to detect bursting around the edges of the large particles. However, no such bursting was observed through either automated burst localization or manual selection of ROIs atop or around the large Sm_2O_3NP. This image analysis protocol has been successfully utilized to both detect bursting atop highly scattering niobium oxide based catalysts[38] (λ_{Ex} = 633 nm) and to rule out acid-catalysis by large Sm_2O_3NP[22] (λ_{Ex} = 488 nm) in another system. Therefore, bursting (and thus formation of **4)** does not occur at the large, visible Sm_2O_3NP but is highly localized, consistent with the explanation that heterogeneous catalysis occurs solely at the locations of the nanometric particles. This conclusion is supported by bench scale experiments in which the same yield of **4** was obtained when starting from either the polydisperse nanomaterial or by first isolating and utilizing the small Sm_2O_3NP for catalysis (see Table 1 entries **d** vs. **j**, **h** vs. **i** and associated discussion).

Mechanistic Investigation. In addition to providing additional evidence that heterogeneous catalytic oxidation of compound **1** is restricted to the surfaces of the small Sm_2O_3NP, a final TIRFM experiment was designed in order to gain further insight into the overall catalytic

mechanism. Based on the results of bench scale experiments (i.e. inability to isolate **[2]$_s$** and spectroscopic evidence of a coumarin-type structure possessing an emission band between those of **1** and a synthetically prepared free aldehyde **2**), as well as on single molecule studies indicating that the Sm_2O_3NP-catalyzed oxidation of **1** is indeed a surface process, we considered the possibility that an activated alcohol species is formed exclusively on the nanometric particle surface as a direct product of the catalysis and that this species **[2]$_s$** is then intercepted by **3**, generating **4** without free aldehyde mediation. A unique advantage of the flow reactor cell used to perform TIRFM is the ability to seamlessly change the reagent solution without disturbing the microscope optics or displacing the sample, allowing the same sample area to be imaged under various experimental conditions. We were thus able to achieve a realistic depiction of the catalytic process by performing a sequential dual-colour TIRFM experiment.

In brief, we flowed a 5 nM solution of **1** over a glass coverslip spin-coated with Sm_2O_3NP and imaged the sample using 488 nm laser excitation and a 550 nm long pass emission filter (Figure 3A1). Without disturbing the sample or altering the microscope optics, we then switched the excitation wavelength to 633 nm and, using a 676/29 nm band pass emission filter, recorded a second image sequence while flowing a 5 nM solution of **3** over the activated sample (Figure 3B1). By comparing the coordinates in which catalytic activity was detected under the two sets of experimental conditions, we observed distinct regions of activity common to both image sequences. Figure 3A1 and B1 are still frame images from the two image sequences, with yellow boxes highlighting two regions of interest that are common to each image. As shown by the corresponding fluorescence intensity-time trajectories, bursting events in these distinct regions are examples of **1** being activated to **[2]$_s$** on small Sm_2O_3NP (Figure 3A2-3), and subsequent condensation of the surface bound activated species with **3** to generate **4** (Figure

3B2-3) in identical locations. The correlation experiment confirms that full formation of **4** is observed wherever the hydroxyl-substituted reagent **1** is partially oxidized to $[\mathbf{2}]_s$, demonstrating that the catalysis is a heterogeneous coupled process in which both reactions leading to **4** occur at the surfaces of the small, catalytically active Sm_2O_3NP.

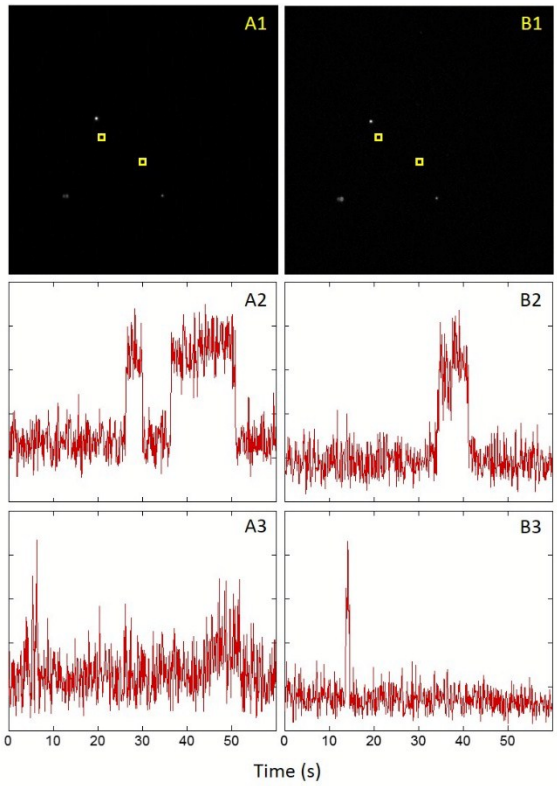

Figure 3 Spatial colocalization of the activation of **1** and the generation of **4**. Single frames of TIRFM image sequences of (**A1**) emission from activated alcohol imaged with excitation at 488 nm and a 550 nm long pass filter and (**B1**) emission from **4** resulting from condensation between $[\mathbf{2}]_s$ and the indolium cation **3** imaged with excitation at 633 nm and a 676/29 nm band pass filter. Yellow boxes highlight the coordinates of identical 3×3 pixel regions of interest in the two images, from which the corresponding fluorescence intensity trajectories (**A2-3** and **B2-3**) of single catalytic spots showing stochastic on/off-events were derived. The trajectories show that activity resulting from the Sm_2O_3NP-catalyzed surface activation of **1** (**A2** and A**3**) occurs in the same location as bursting originating from **4** (**B2** and **B3**).

Discussion

Investigating the catalytic mechanism at the single molecule level points to a strictly surface-localized catalytic process in which a direct product of the catalysis (species $[\mathbf{2}]_s$) is formed exclusively on the nanometric particle surface and is then intercepted by **3**, generating **4** without free aldehyde mediation. A tentative mechanism is illustrated in Figure 4, showing the oxidation of **1** and condensation of $[\mathbf{2}]_s$ with **3** as coupled processes involving an partially oxidized activated alcohol on the Sm_2O_3NP surface.

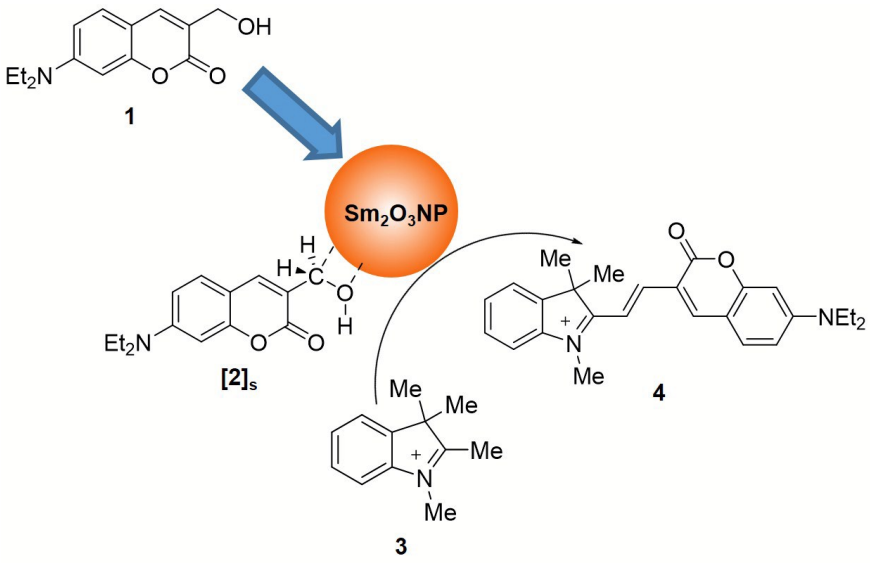

Figure 4 Proposed mechanism for the overall catalytic process. The heterogeneously-catalyzed oxidation of **1** occurs exclusively at the surfaces of small Sm_2O_3NP and is followed by condensation of the surface bound partially oxidized activated alcohol $[\mathbf{2}]_s$ with **3** to generate the emissive product **4**.

This behavior resembles that of ruthenium nanoparticles (RuNP) supported on mesoporous silica that we proposed as a heterogeneous catalyst for oxidative Wittig coupling reactions.[17] In our report, we observed that the Wittig olefination product using benzyl alcohol as starting material occurs without the intermediacy of the aldehyde (the common Wittig substrate). Thus, we proposed the alcohol oxidation and the olefination as codependent processes coupled on the

surfaces of RuNP. Inspired by these considerations, we tested our Sm_2O_3NP as a heterogeneous catalyst for the Wittig olefination of benzyl alcohol with, and without the Wittig reagent methyl(triphenylphosphoranylidene)acetate. In stunning resemblance to the behavior of supported RuNP, gas-chromatography results (Figure S11, Supporting Information) show the olefination product (methyl cinnamate) only in the presence of the Wittig reagent, while the aldehyde supposedly generated by the single oxidation of benzyl alcohol was not observed. Not only does this demonstrate that the scope of Sm_2O_3NP-catalyzed redox chemistry extends beyond the synthesis of **4**, samarium is more readily abundant than ruthenium and thus a more desirable material in the move toward sustainable catalysis. Indeed, Sm_2O_3NP-based nanomaterials may represent a starting point in the development of a generally applicable heterogeneous catalyst for sustainable one-pot aldehyde chemistry.

Conclusion

We have reported on the first utilization of Sm_2O_3NP for purely heterogeneous redox catalysis in one-pot aldehyde chemistry. The catalyst shows promise in multiple reactions involving aldehydes (e.g. Wittig chemistry), allows one to begin with a less expensive and more readily-prepared alcohol precursor and is unaffected by undesirable over-oxidation to the corresponding carboxylic acid. We have shown that Sm_2O_3NP efficiently activate the hydroxyl-functionalized starting material for a subsequent *in situ* enamine-type condensation but that the reaction proceeds without the intermediacy of a freely diffusing aldehyde. Examining the system at the single molecule level was critical to uncovering this interesting aspect of the catalytic mechanism, and highlighted the enhanced understanding that can be achieved using single molecule techniques for catalysis research. Such methods are no longer solely the realm of biology; their applicability in mainstream inorganic chemistry and nanomaterials science has

spread dramatically and is being realized at a new higher level. In this case, a supramolecular strategy was implemented based on information provided by a previous single molecule study in order to achieve the full benefit of pure heterogeneous catalysis and also facilitated the elucidation of the interesting catalytic mechanism using single molecule fluorescence microscopy. TIRFM unequivocally established that small Sm_2O_3NP catalyze the activation of the alcohol on their surfaces and demonstrated that the coupled processes proceed through a heterogeneous catalytic mechanism. Such insight into the mode of catalysis at work and the reactive species involved is essential to the evaluation of new nanomaterials and could only be obtained by studying the catalysis at the molecular level, where traditional ensemble-averaged experiments proved inadequate. This work showcases the opportunity provided by single molecule techniques when applied to catalysis research, including the benefit of progression *'from the molecule to mole'* – a bottom-up approach in which knowledge obtained through single molecule studies is used to improve scaled up catalyst performance as part of an iterative design process.

Methods

Materials. Sm_2O_3NP were prepared and characterized according to our previously published protocol.[28] The synthesis of compounds **1**, **2**, **3** and **4** is described in the Supporting Information.

Experimental. Acetonitrile (MeCN) was purified with a LC Technology Solutions Inc. SPBT-1 Bench Top Solvent Purification System. Chemicals were purchased from Sigma-Aldrich or Fisher Scientific. All the reactions were monitored by thin-layer chromatography, using aluminum sheets coated with silica (60, F_{254}). NMR spectra were recorded at room temperature with a Bruker Avance 300 spectrometer. Mass spectral analysis was performed with a 6890N

Network GC System equipped with a 5973 Mass Selective Detector from Agilent Technologies. ESI mass spectra in positive mode were acquired with a Micromass Q-TOF I. High-resolution EI mass spectra were acquired with a HRes, Concept S1, Magnetic Sector mass spectrometer and were conducted in the John L. Holmes Mass Spectrometry Facility at the Department of Chemistry and Biomolecular Sciences, University of Ottawa. Emission spectra were recorded with a PTI spectrofluorometer. Absorbance spectra were recorded using a Cary 50 UV−visible spectrophotometer. For the UV-Vis analysis of reactions **a-j**, the catalyst (when present) was separated by centrifugation and washed three times with EtOH. The combined supernatants were dried under reduced pressure, redissolved in 2 mL of EtOH and further diluted 100 fold. For each sample, the concentration of **4** was calculated by absorption values at λ = 575 nm. The molar extinction coefficient of **4** in EtOH at λ = 575 nm was calculated by performing a calibration curve with known concentrations of **4** and was estimated at 14218 M^{-1} cm^{-1}.

Single Molecule Fluorescence Microscopy. Glass coverslips (25 mm, Fisher) were cleaned by soaking in piranha solution for 30 min followed by thorough washing with MilliQ H_2O (18.2 MΩ cm^{-1} at 25 °C; 0.22 μm filter), then dried with argon. Sm_2O_3NP were dispersed in EtOH (0.05 mg/mL) and deposited on a clean coverslip through spin coating (50μL, 1000 rpm, 90 s). The Sm_2O_3NP-catalyzed formation of **4** was analyzed by flowing equimolar solutions of **1** and **3** in EtOH at 1 mL h^{-1} through a flow cell reactor (Chamlide model CF-S25-B) over the catalyst-loaded microscope coverslip. Fluorescence imaging was performed with an Olympus FV1000 TIRF (Olympus, Japan). The instrument is equipped with a 488 nm Ar laser (CW), a 633 nm He-Ne laser (CW) and an EM-CCD (Rolera EM-C2, Q-Capture). The laser beam was collimated and focused through a fibre-coupling unit. The microscope is equipped with an oil-immersion TIR (total internal reflection) objective (×100, NA 1.45, Olympus, PLAPO). A 550 nm long pass

(Semrock) or a Chroma ET655 emission filters (676/29 nm band pass) were used to monitor bursting events at the single molecule level. The fluorescence spectrum of **4** was recorded with a Fluorescent Lifetime Imaging system (MicroTime 200, PicoQuant, Berlin, Germany). The instrument is equipped with a frequency doubled, picosecond pulse diode laser (637 nm, 93 ps, 40 MHz, LDH-P-FA-640L; PicoQuant). A beam splitter (Z638rdc, Chroma) was used to separate excitation and emission light. The emission signal was collected by a Shemrock SR-163 spectrograph (Andor Technology, South Windsor, USA) using a 690/70 nm band pass emission filter. Fluorescence microscope images and TIRFM image sequences were analyzed using ImageJ (NIH) and MatLab. Stochastic bursting events in TIRFM image sequences were identified and labeled as 3×3 pixel regions of interest. ImageJ was then used to perform scattering subtraction (rolling ball algorithm, 10 pixel radius) before measuring the mean fluorescence intensity in each region of interest for every frame in a TIRFM image sequence. These data were then used to generate intensity vs. time trajectories using OriginLab software.

References

1. P. Chen, X. Zhou, H. Shen, N. M. Andoy, E. Choudhary, K.-S. Han, G. Liu and W. Meng, *Chem. Soc. Rev.*, 2010, **39**, 4560-4570.
2. P. Chen, X. Zhou, N. M. Andoy, K.-S. Han, E. Choudhary, N. Zou, G. Chen and H. Shen, *Chem. Soc. Rev.*, 2014, **43**, 1107-1117.
3. I. L. C. Buurmans and B. M. Weckhuysen, *Nature Chem.*, 2012, **4**, 873-886.
4. T. Cordes and S. A. Blum, *Nature Chem.*, 2013, **5**, 993-999.
5. K. P. F. Janssen, G. De Cremer, R. K. Neely, A. V. Kubarev, J. Van Loon, J. A. Martens, D. E. De Vos, M. B. J. Roeffaers and J. Hofkens, *Chem. Soc. Rev.*, 2014, **43**, 990-1006.
6. N. M. Esfandiari, Y. Wang, J. Y. Bass, T. P. Cornell, D. A. L. Otte, M. H. Cheng, J. C. Hemminger, T. M. McIntire, V. A. Mandelshtam and S. A. Blum, *J. Am. Chem. Soc.*, 2010, **132**, 15167-15169.
7. X. Zhou, E. Choudhary, N. M. Andoy, N. Zou and P. Chen, *ACS Catal.*, 2013, **3**, 1448-1453.
8. R. Ameloot, M. Roeffaers, M. Baruah, G. De Cremer, B. Sels, D. De Vos and J. Hofkens, *Photochem. Photobiol. Sci.*, 2009, **8**, 453-456.
9. S. A. Blum, *Phys. Chem. Chem. Phys.* , 2014, **16**, 16333-16339.

10. G. De Cremer, M. B. J. Roeffaers, E. Bartholomeeusen, K. Lin, P. Dedecker, P. P. Pescarmona, P. A. Jacobs, D. E. De Vos, J. Hofkens and B. F. Sels, *Angew. Chem. Int. Ed.* , 2010, **49**, 908-911.
11. Q. T. Easter, V. Trauschke and S. A. Blum, *ACS Catal.*, 2015, **5**, 2290-2295.
12. W. Luo, M. Sankar, A. M. Beale, Q. He, C. J. Kiely, P. C. A. Bruijnincx and B. M. Weckhuysen, *Nat. Commun.*, 2015, **6**.
13. Z. Ristanović, J. P. Hofmann, G. De Cremer, A. V. Kubarev, M. Rohnke, F. Meirer, J. Hofkens, M. B. J. Roeffaers and B. M. Weckhuysen, *J. Am. Chem. Soc.*, 2015, **137**, 6559-6568.
14. Z. Ristanović, M. M. Kerssens, A. V. Kubarev, F. C. Hendriks, P. Dedecker, J. Hofkens, M. B. J. Roeffaers and B. M. Weckhuysen, *Angew. Chem. Int. Ed.*, 2015, **54**, 1836-1840.
15. M. B. J. Roeffaers, G. De Cremer, J. Libeert, R. Ameloot, P. Dedecker, A.-J. Bons, M. Bückins, J. A. Martens, B. F. Sels, D. E. De Vos and J. Hofkens, *Angew. Chem. Int. Ed.*, 2009, **48**, 9285-9289.
16. L. Su, G. Lu, B. Kenens, S. Rocha, E. Fron, H. Yuan, C. Chen, P. Van Dorpe, M. B. J. Roeffaers, H. Mizuno, J. Hofkens, J. A. Hutchison and H. Uji-i, *Nat. Commun.*, 2015, **6**.
17. A. I. Carrillo, L. C. Schmidt, M. L. Marin and J. C. Scaiano, *Catal. Sci. Technol.* , 2014, **4**, 435-440.
18. W. Xu, J. S. Kong, Y.-T. E. Yeh and P. Chen, *Nature Mater.*, 2008, **7**, 992-996.
19. A. Rybina, C. Lang, M. Wirtz, K. Grußmayer, A. Kurz, F. Maier, A. Schmitt, O. Trapp, G. Jung and D. P. Herten, *Angewandte Chemie International Edition*, 2013, **52**, 6322-6325.
20. I. W. Davies, L. Matty, D. L. Hughes and P. J. Reider, *J. Am. Chem. Soc.* , 2001, **123**, 10139-10140.
21. C. D. McTiernan, S. P. Pitre and J. C. Scaiano, *ACS Catal.*, 2014, **4**, 4034-4039.
22. G. K. Hodgson, S. Impellizzeri and J. C. Scaiano, *Chem. Sci.* , 2016, **7**, 1314-1321.
23. L. Chen, G. Chen, C.-F. Leung, S.-M. Yiu, C.-C. Ko, E. Anxolabéhère-Mallart, M. Robert and T.-C. Lau, *ACS Catal.*, 2015, **5**, 356-364.
24. J. Oliver-Messeguer, L. Liu, S. García-García, C. Canós-Giménez, I. Domínguez, R. Gavara, A. Doménech-Carbó, P. Concepción, A. Leyva-Pérez and A. Corma, *J. Am. Chem. Soc.*, 2015, **137**, 3894-3900.
25. N. M. Esfandiari and S. A. Blum, *J. Am. Chem. Soc.*, 2011, **133**, 18145-18147.
26. E. M. Hensle and S. A. Blum, *J. Am. Chem. Soc.*, 2013, **135**, 12324-12328.
27. M. R. Decan, S. Impellizzeri, M. L. Marin and J. C. Scaiano, *Nat. Commun.*, 2014, **5**.
28. G. K. Hodgson, S. Impellizzeri, G. L. Hallett-Tapley and J. C. Scaiano, *RSC Adv.*, 2015, **5**, 3728-3732.
29. Z. Jiang, W. Zhou, D. Tan, R. Zhai and X. Bao, *Surf. Sci.* , 2004, **565**, 269-278.
30. M. Juel, B. T. Samuelsen, M. Kildemo and S. Raaen, *Surf. Sci.*, 2006, **600**, 1155-1159.
31. M. Kuchowicz and J. Kołaczkiewicz, *Surf. Sci.*, 2008, **602**, 3721-3727.
32. T.-D. Nguyen, C.-T. Dinh and T.-O. Do, *Langmuir*, 2009, **25**, 11142-11148.
33. T.-D. Nguyen, C.-T. Dinh, D.-T. Nguyen and T.-O. Do, *J. Phys. Chem. C*, 2009, **113**, 18584-18595.
34. T.-D. Nguyen, D. Mrabet and T.-O. Do, *J. Phys. Chem. C*, 2008, **112**, 15226-15235.
35. Q. Xu, S. Hu, D. Cheng, X. Feng, Y. Han and J. Zhu, *J. Chem. Phys.*, 2012, **136**, 154705.
36. D. Cheng, Q. Xu, Y. Han, Y. Ye, H. Pan and J. Zhu, *J. Chem. Phys.* , 2014, **140**, 094706.
37. E. Deniz, S. Sortino and F. M. Raymo, *J. Phys. Chem. Lett.* , 2010, **1**, 3506-3509.

38. S. Impellizzeri, S. Simoncelli, C. Fasciani, M. Luisa Marin, G. L. Hallett-Tapley, G. K. Hodgson and J. C. Scaiano, *Catal. Sci. Technol.*, 2015, **5**, 169-175.
39. R. Hudson, C.-J. Li and A. Moores, *Green Chem.*, 2012, **14**, 622-624.

Acknowledgements

The Natural Sciences and Engineering Research Council of Canada supported this work through its Discovery program, while the Canada Foundation for Innovation enabled the purchase of the instrumentation used in this work. G. K. Hodgson acknowledges the award of an Ontario Graduate Scholarship. Thanks are due also to the Government of Canada and NSERC for a Banting Postdoctoral Fellowship to S. Impellizzeri.

Author Contributions

S. I. and G. K. H. made equal contributions to the experimental work, data analysis and to writing the manuscript. J. C. S. supervised the research and contributed to project discussions as well as the manuscript.

Additional Information

Supplementary Information: Synthetic protocols, absorption and emission spectra, SEM images of Sm_2O_3NP before and after bench scale reactions, representative intensity-time trajectories showing background scattering under various experimental conditions, widefield transmission image of Sm_2O_3NP spin-coated onto a microscope coverslip, proposed mechanism and gas chromatograms for Sm_2O_3NP-catalyzed alcohol oxidation and Wittig olefination as coupled processes, representative TIRFM image sequence, TIRFM image sequences.

Competing financial interest: The authors declare no competing financial interest.

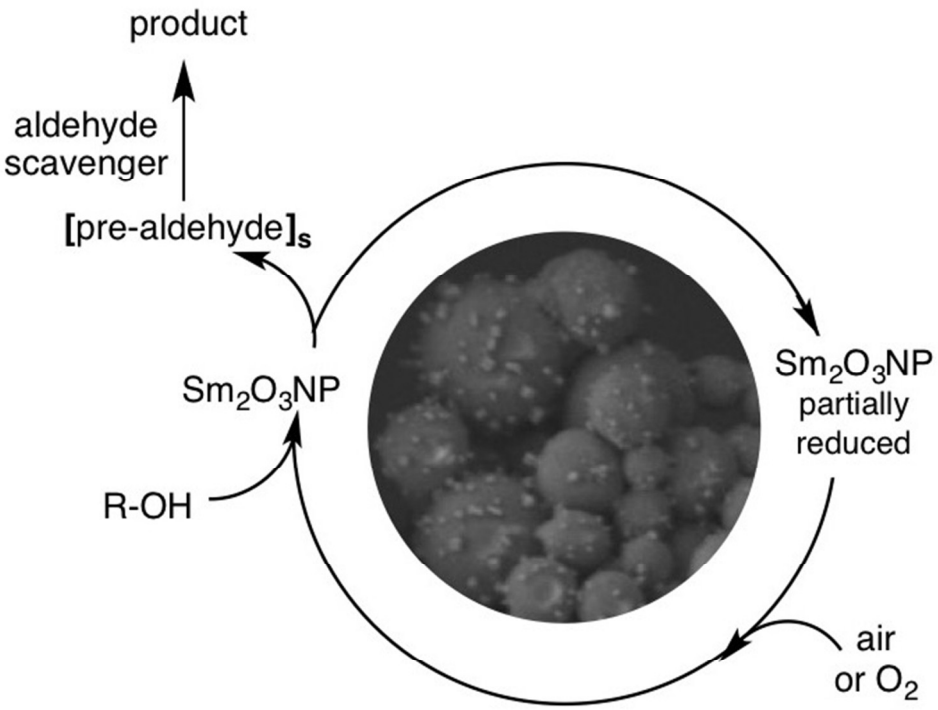

253x195mm (72 x 72 DPI)